nature communications

Article

https://doi.org/10.1038/s41467-025-60377-1

Quantum spin Hall effect in magnetic graphene

Received: 28 October 2024

Accepted: 12 May 2025

Published online: 24 June 2025

Check for updates

Talieh S. Ghiasi[1,2] ✉, Davit Petrosyan[1], Josep Ingla-Aynés[1], Tristan Bras[1], Kenji Watanabe[3], Takashi Taniguchi[4], Samuel Mañas-Valero[1,5], Eugenio Coronado[5], Klaus Zollner[6], Jaroslav Fabian[6], Philip Kim[2] & Herre S. J. van der Zant[1]

A promising approach to attain long-distance coherent spin propagation is accessing topological spin-polarized edge states in graphene. Achieving this without external magnetic fields necessitates engineering graphene band structure, obtainable through proximity effects in van der Waals heterostructures. In particular, proximity-induced staggered potentials and spin-orbit coupling are expected to form a topological bulk gap in graphene with gapless helical edge states that are robust against disorder. In this work, we detect the spin-polarized helical edge transport in graphene at zero external magnetic field, allowed by the proximity of an interlayer antiferromagnet, $CrPS_4$. We show the coexistence of the quantum spin Hall (QSH) states and magnetism in graphene, where the induced spin-orbit and exchange couplings also give rise to a large anomalous Hall (AH) effect. The detection of the QSH states at zero external magnetic field, together with the AH signal that persists up to room temperature, opens the route for practical applications of magnetic graphene in quantum spintronic circuitries.

Decades of research in graphene have unveiled its remarkable charge and spin-related properties, such as distinctive quantum Hall (QH) charge transport and long-distance spin propagation[1,2]. Yet, harnessing topologically protected spin transport for the development of practical quantum spintronic devices necessitates targeted modifications to the graphene band structure. This band structure engineering has been recently achieved non-invasively by bringing graphene in the proximity of other two-dimensional (2D) materials[3], leading to spin Hall[4,5], Rashba-Edelstein[6–8], anomalous Hall (AH)[9], and spin-dependent Seebeck[10] effects in graphene. The realization of these phenomena in proximitized graphene is due to induced spin-orbit and/or exchange interactions that result in spin-splitting of the graphene band structure[11–13]. These spin-related effects, however, have been experimentally addressed in proximitized graphene majorly by diffusive charge/spin transport, where the spin relaxation length is limited by spin and momentum scattering mechanisms. On the contrary, if the transport occurs through topological spin-polarized edge states, their topological protection allows for long-distance quantum coherent spin propagation.

Spin-polarized chiral and helical QH edge states have been detected in graphene through the Zeeman splitting of the bands by applying large magnetic fields[14–16], which is conceived to be practically challenging for applications. Thus, numerous theoretical and experimental reports so far focus on resolving spin-polarized edge states in graphene without the need for any external magnetic field, possible through the emergence of quantum spin Hall (QSH) or quantum anomalous Hall (QAH) states in a modified graphene band structure[17–28]. These spin-polarized gapless edge states can form within the bulk gap of graphene, attainable by inducing staggered potentials, spin-orbit coupling (SOC) and/or magnetic exchange interactions[17–19].

[1]Kavli Institute of Nanoscience, Delft University of Technology, Delft, The Netherlands. [2]Department of Physics, Harvard University, Cambridge, Massachusetts, USA. [3]Research Center for Electronic and Optical Materials, National Institute for Materials Science, Tsukuba, Japan. [4]Research Center for Materials Nanoarchitectonics, National Institute for Materials Science, Tsukuba, Japan. [5]Institute of Molecular Science, University of Valencia, Paterna, Spain. [6]Institute for Theoretical Physics, University of Regensburg, Regensburg, Germany. ✉e-mail: t.s.ghiasi@tudelft.nl

Depending on the respective magnitude of the spin-orbit vs. exchange interactions, these edge states can be chiral or helical[20], allowing for topologically protected spin transport that is expected to be robust against disorder[18].

Despite several recent experimental efforts in addressing the topological transport in various graphene-based van der Waals heterostructures[29–34], direct experimental evidence for the detection of the QAH and QSH effects in proximitized graphene is still missing. One major obstacle has been the presence of dominant interfacial charge transfer[35,36] that may hinder the exploration of the proximity effects. In this work, however, the suppression of the interfacial charge transfer in graphene-$CrPS_4$ heterostructures allows us to study the transport in the presence of magnetic exchange and spin-orbit interactions, evidenced by the detection of a large AH signal up to room temperature. Remarkably, we experimentally realize the presence of helical states at zero external magnetic field, indicating the emergence of the QSH effect despite the breaking of time-reversal symmetry by the induced magnetism[20,37]. The unprecedented zero-magnetic-field detection of the QSH state in this graphene-based magnetic heterostructure, coexisting with the AH effect, makes this system intriguing for the development of quantum spintronic circuitries.

Results

We bring graphene in the van der Waals proximity of the interlayer antiferromagnet, $CrPS_4$ (CPS), which is an air-stable semiconductor with a bandgap of ~1.3 eV[38] and a Néel temperature $T_N \approx 38$ K[39]. Figure 1a (top panel) illustrates a top view of the CPS crystal structure with the dashed lines indicating the crystallographic directions along which the crystals preferentially cleave, as shown in the optical micrograph of an exfoliated flake. As a result, the CPS flakes acquire a corner angle of 67.5°, the bisector of which is along the magnetic a-axis[38] (see also supplementary information (SI), Figure S2). The presence of this characteristic angle assists with the identification of

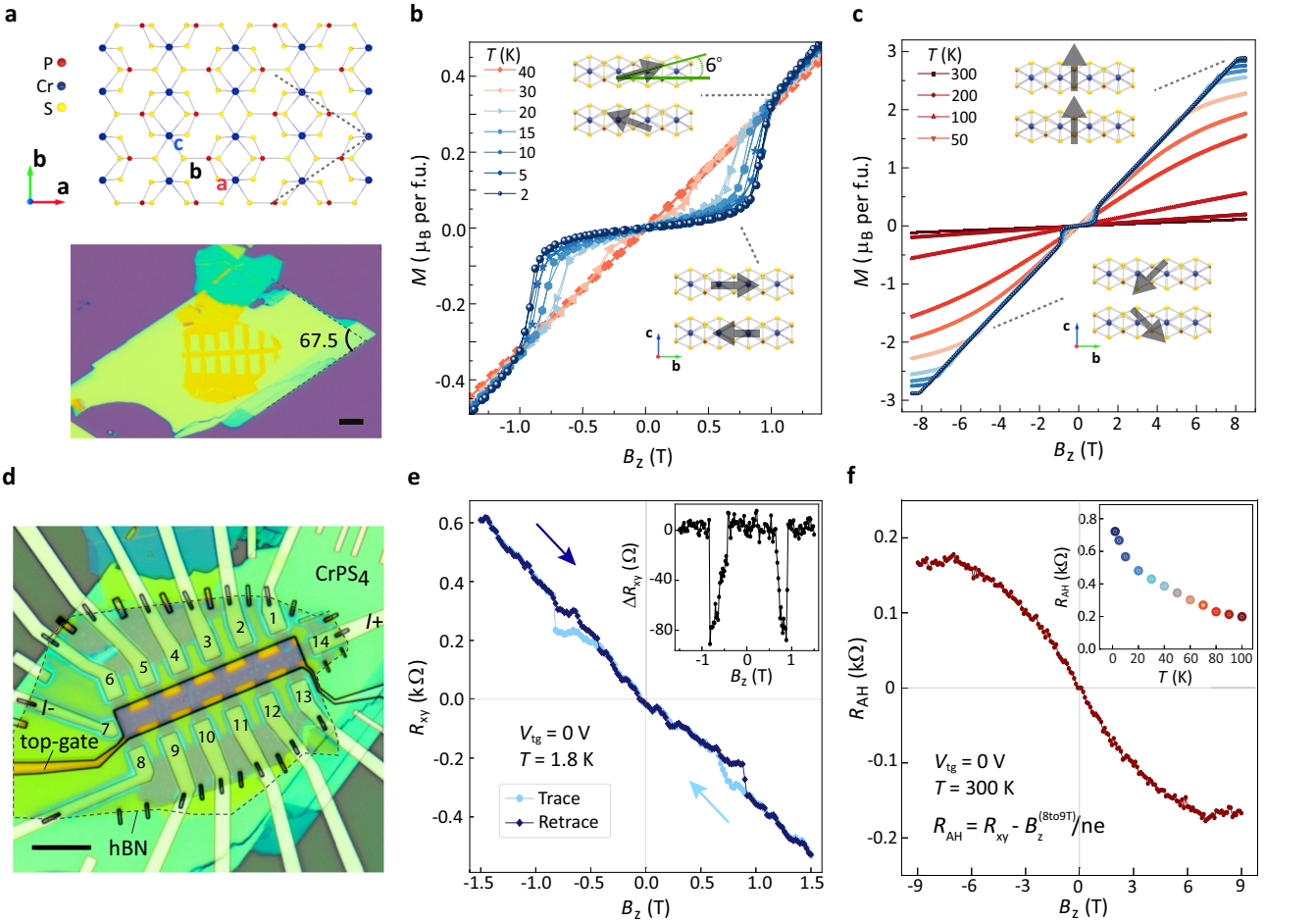

Fig. 1 | $CrPS_4$ (CPS) magnetic ordering and induced magnetism in graphene. **a** Top-view ($a-b$ plane) schematic of monoclinic CPS crystal structure (space group C2[51]). The optical micrograph (scale bar: 10 μm) shows a 38 nm thick CPS flake covered with an hBN/graphene Hall-bar (see SI, Figure S1). **b**, **c** SQUID magnetometry of a CPS bulk crystal at various temperatures (T) for small (**b**) and large (**c**) range of magnetic field B_z, applied perpendicular to the ($a-b$) plane. The B_z cycling shows a minimal hysteresis in CPS bulk magnetization. Insets: side-view schematics of CPS layers magnetic ordering at indicated B_z ranges. **d** Optical micrograph of device A fabricated with an hBN/graphene/CPS heterostructure on a SiO_2/Si substrate with Ti-Pd electrodes. Scale bar: 10 μm. The hBN and SiO_2 layers, used as top- and back-gate dielectrics, are 73 and 285 nm thick, respectively. **e** Transverse resistance $R_{xy} = V_{xy}/I$ measured vs. B_z in the graphene Hall-bar at $T = 1.8$ K with $I = 0.5$ μA, at back-gate and top-gate voltages of $V_{bg} = 50$ V and $V_{tg} = 0$ V. The non-linearity of R_{xy} at $B_z < 1$ T is due to non-linear CPS magnetization behaviour in that B_z range (see Figure S4). Inset: subtraction of the trace and retrace measurements (ΔR_{xy}), showing the R_{xy} modulation due to spin-flop transition. The asymmetry in the ΔR_{xy} vs. B_z arises from non-symmetric magnetization behavior of the outmost CPS layer through the spin-flop transition, likely caused by neighboring magnetic domains in the CPS flake. **f** Non-linear component of R_{xy} associated with the AH effect (R_{AH}), measured at $T = 300$ K, $V_{bg} = 50$ V and $V_{tg} = 0$ V. R_{AH} is acquired by subtraction of a linear background (related to the ordinary Hall effect) from R_{xy} anti-symmetrized vs. B_z (also see SI Figure S3). For the linear fit, the R_{xy} data in the range of $8\,T < B_z \leq 9\,T$ is considered, assuming saturation of the magnetization in that range. Inset: Temperature-dependence of R_{AH} at $V_{tg} = 0$ V. The R_{AH} is estimated as the lower bound, averaged over the R_{AH} for $B_z > 6$T (see SI, section 4).

https://doi.org/10.1038/s41467-025-60377-1

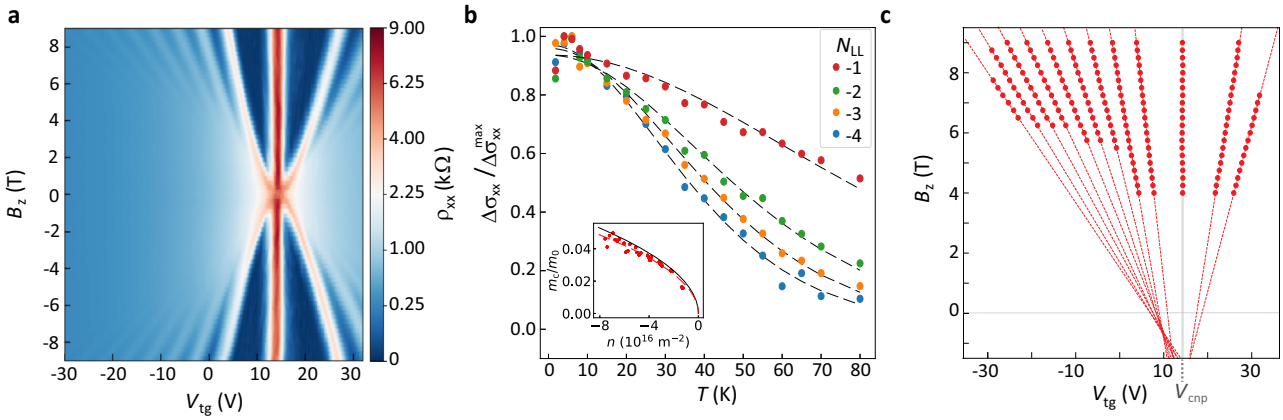

Fig. 2 | Quantum Hall transport in magnetized graphene. a Shubnikov-de Haas oscillations of the longitudinal resistivity ρ_{xx} in graphene, measured vs. applied top-gate voltage and magnetic field (using voltage probes V_5 and V_6, shown in Fig. 1d). **b** Amplitude of the SdHOs ($\Delta\sigma_{xx}$) for LL number of $N_{LL} = -1$ to -4 as a function of T, normalized to their maxima. Dashed lines are the fits to the data using $\Delta\sigma_{xx} = T/\sinh(2\pi^2 k_B T m_c/\hbar e B_z)$. Inset: cyclotron mass, m_c, extracted from all the hole-like LLs, plotted as the ratio with respect to the electron rest mass (m_0) vs. carrier density (n). The red curve is a fit to the extracted m_c/m_0 vs. n, considering a linear dispersion relation, resulting in Fermi velocity, $v_F \approx 1.196 \times 10^6$ m/s. The black curve is the theoretically expected behavior for pristine graphene with $v_F = 1.1 \times 10^6$ m/s. The effective n in the graphene channel is extracted from Hall measurements (for $B_z \geq 8$ T), and separately from the dependence of B_z vs. V_{tg} for each LL. These two approaches give rise to similar extracted values for n (see SI, Section 8). **c** Landau fan diagram: the red dots are the maxima of the ρ_{xx} vs. V_{tg} extracted from panel a for gate voltages slightly away from the charge neutrality point ($|V_{tg} - V_{cnp}| > 5$ V), with the red dashed lines as linear fits.

the CPS crystallographic orientation and guides the alignment of the graphene Hall bar with one of the CPS magnetic axes (see Figure 1a, lower panel). In accordance with previous reports[39], CPS has an anisotropic magnetic behavior which is evaluated using a superconducting quantum interference device (SQUID) at various temperatures (T), shown in Fig. 1b and c (see Methods for more details on CPS). The SQUID measurements at the small-range B_z (panel b) for $T < 40$ K show the expected spin-flop transition when the magnetization of the layers rotates from canted out-of-plane towards the in-plane b-axis, while holding their respective antiparallel alignment (lower inset in Fig. 1b). Increasing B_z above the spin-flop transition field (B_{sf} ~ 0.8 T at 2 K) results in canting of the magnetic moments towards the c-axis, starting with ~6° canting (upper inset in panel b) until full saturation (90°) at $B_z \approx 8$ T, as shown in Fig. 1c.

We evaluate the possibility of inducing the CPS magnetic properties in graphene by transport measurements. We report on four devices (A-D), each fabricated with a monolayer graphene Hall-bar on a multilayer CPS flake, fully covered with hBN that is used as a dielectric for top-gating (Fig. 1d). In devices A, B, and C, the graphene channel is aligned with the CPS magnetic a-axis. We apply current along the graphene channel (with $I+$ and $I-$ electrodes shown in panel d) while measuring the longitudinal and transverse voltages (V_{xx} and V_{xy}). In Fig. 1e, we show the modulation of the transverse resistance $R_{xy} = V_{xy}/I$ as a function of B_z, at $V_{tg} = 0$ V. In addition to the slight non-linear behaviour at $|B_z| < 1$ T (also see Figure S4), we observe switches in R_{xy} at ~ ± 0.8 T, which is the magnetic field at which the spin-flop transition occurs in CPS (B_{sf}). This is a direct indication that the magnetic behavior of the CPS influences the charge transport in graphene, which is detected here by the AH effect.

The trace and retrace measurements of R_{xy} in Fig. 1e show no hysteresis vs. B_z, except for B_z close to B_{sf}. This hysteresis is absent in the SQUID measurements of the bulk crystal, implying the sensitivity of the AH effect to the behaviour of the magnetization of the outermost layer of the CPS ($\mathbf{M}_{CPS}$). Under applied B_z, the behavior of $\mathbf{M}_{CPS}$ is expected to be ruled by its antiferromagnetic coupling with respect to the other CPS layers, and yet, the lack of a neighboring CPS layer on top can cause the $\mathbf{M}_{CPS}$ to lag behind the magnetization dynamics of the bulk of CPS, leading to the observed hysteresis. By decreasing B_z, $\mathbf{M}_{CPS}$ undergoes a spin-flop transition at ~0.5 T, by which R_{xy} in the retrace retrieves its initial value as in the trace measurement. The difference of R_{xy} in the trace and retrace measurements is about 80 Ω (shown in the inset of Fig. 1e), which is the AH effect signal generated by the spin-flop transition of the $\mathbf{M}_{CPS}$.

The AH resistance (R_{AH}) is dependent on the projection of the magnetization $\mathbf{M}_{CPS}$ along the c-axis. From the comparison of the magnetization values measured by SQUID at B_z ~ 0.8 and 8 T (in Fig. 1c), one can tell that through the spin-flop transition, the $\mathbf{M}_{CPS}$ cants towards the c-axis only by 6 degrees, which has led to $R_{AH} \approx 80$ Ω. Considering that and the linear relation between the R_{AH} and z-component of $\mathbf{M}_{CPS}$, R_{AH} should be about 700 Ω when $\mathbf{M}_{CPS}$ is fully saturated out-of-plane, consistent with the value we measure at large B_z (see SI, Figure S5). Further evaluation of the AH effect at various temperatures is shown in Fig. 1f (inset), indicating a considerable decay vs. T. Yet, there is a finite value of R_{AH} of about 150 Ω that persists up to 300 K. Note that at elevated temperatures CPS is a paramagnet, thus a finite magnetic field is required to induce magnetism in graphene. The detected R_{AH} in this heterostructure is larger than that achieved so far in proximitized graphene[9,10,40,41]. The observation of such a sizable R_{AH} is a signature of the co-presence of strong induced spin-orbit and exchange interactions[42] in the proximitized graphene up to room temperature, which is consistent with the recently reported enhancement of the Curie temperature at the graphene-CPS interface[43]. The detection of the unprecedentedly large AH effect in this system is also expected from the strong hybridization between the graphene and CPS bands, shown by our density functional theory (DFT) calculations (see SI, Section 14).

Having established the proximity-induced magnetism in the graphene channel, we explore the QH regime of transport in this system. By cooling down the device, signatures of QH transport become evident at finite B_z, as shown in Fig. 2. Panel a shows the modulation of the longitudinal resistivity (ρ_{xx}) vs. B_z, i.e., the Shubnikov de-Haas oscillations (SdHOs). The back-gate voltage (V_{bg}) is set to 50 V to shift the Dirac point such that the electron-like Landau levels (LLs) are reachable by the top-gating. We evaluate the back-gate vs. top-gate dependence of the LLs in Figure S7, indicating only a shift of the LLs by electrostatic doping without any significant change in the Landau fan diagram with V_{bg} (SI, Figure S8). Moreover, there is a negligible shift of the Dirac peak vs. B_z (SI, Figure S9) and there is a minimal hysteresis for the V_{tg}-dependence of ρ_{xx}, which decreases with raising temperature (SI, Figure S10). These observations are in contrast with recent reports

https://doi.org/10.1038/s41467-025-60377-1

on graphene in the proximity of CrX_3[36] or CrOCl[35], where gate-dependent interfacial charge transfer influences the transport in graphene.

From the QH transport, we obtain the cyclotron mass m_c and the Fermi velocity v_F of the electrons in the magnetized graphene. Having the temperature-dependence of the modulations of the longitudinal conductivity $\Delta\sigma_{xx}$ (see SI, Figure S11b), m_c is extracted by fitting $\Delta\sigma_{xx}$ to the standard expression $T/\sinh(2\pi^2 k_B T m_c/\hbar e B_z)$, with k_B the Boltzmann constant[44,45], shown for the first few hole-like LLs in Fig. 2b. The ratio of the cyclotron mass vs. the rest mass of the electrons (m_c/m_0) extracted from the SdHOs at 8 T < $|B_z|$≤9 T for different carrier density (n) is shown in the inset. The extracted m_c/m_0 ratio and the v_F determined from the fit vs. n show consistency with that expected for the case of pristine graphene with $v_F = 1.1 \times 10^6$ m/s (indicated by the black solid line in the inset)[44,45].

However, the Landau fan diagram in graphene-CPS (Fig. 2a) differs from that of pristine graphene, showing shifts of the LLs in V_{tg} and minimal broadening of the zeroth LL (zLL) vs. B_z. A slight non-linearity of the first Landau fans is present close to zero energy which could be related to a small non-linear dependence of n vs. V_{tg} close to the charge neutrality point (V_{cnp}). This nonlinearity is likely related to a small contribution of CPS localized midgap states in the total capacitance at low density of states in graphene, particularly at large positive V_{tg} when the Fermi energy E_F is expected to get closer to the conduction band edge in the CPS. In Fig. 2c, we show the maxima of ρ_{xx} vs. V_{tg} for $|V_{tg} - V_{cnp}| > 5$ V, together with the linear fits, clearly showing the linear behavior of the Landau fans. That also rules out the dominant contribution of interfacial charge transfer that would cause nonlinearities in Landau fans due to its dependence on magnetic ordering[35,36]. Figure 2c further indicates that the Landau fans do not converge at one

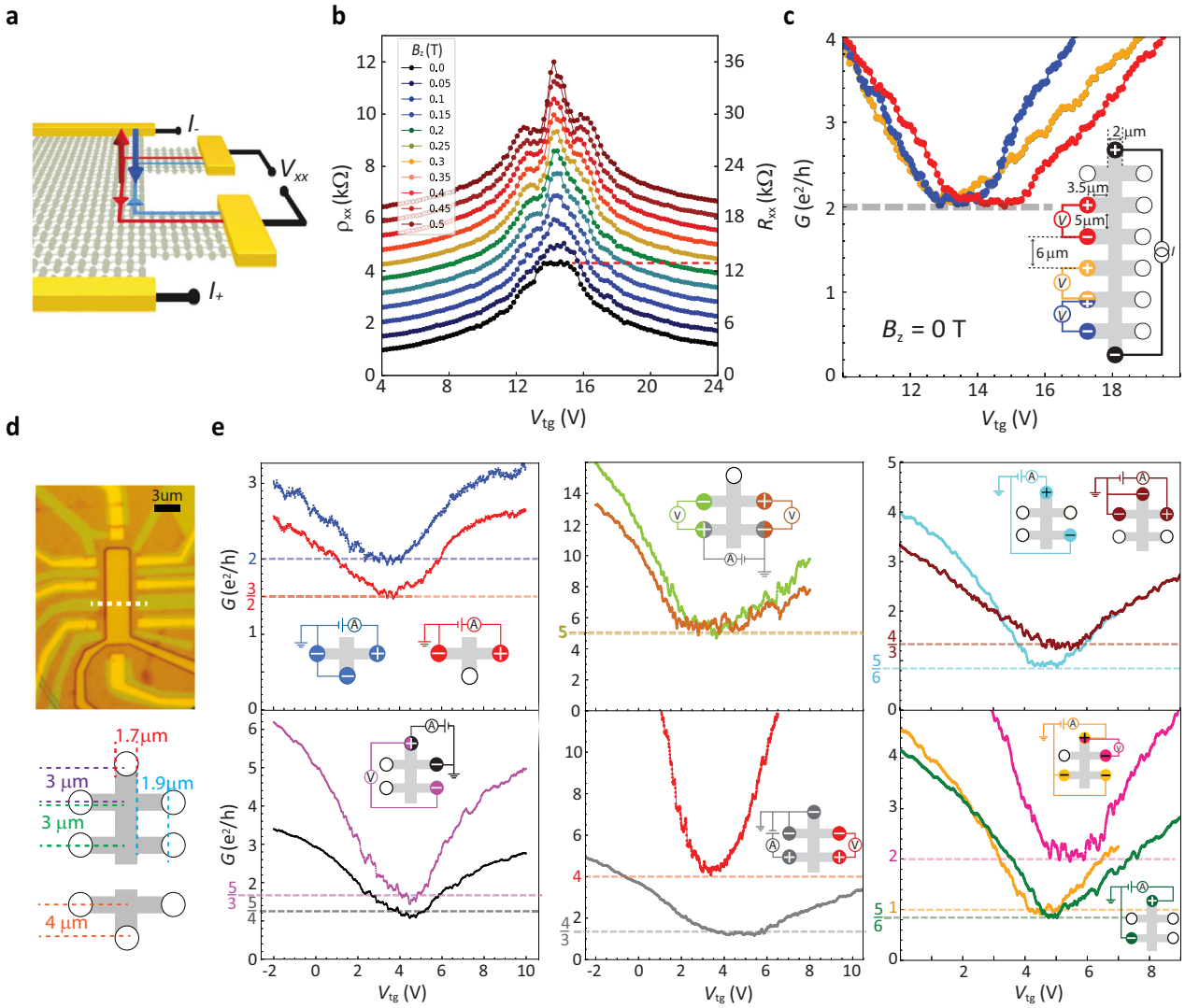

Fig. 3 | Quantum spin Hall states in magnetized graphene near zero energy. a A schematic of the device and a four-terminal measurement geometry are shown with the propagation direction of the helical states at the edge of the graphene channel. **b** V_{tg}-dependence of the graphene resistivity, ρ_{xx}, (left axis), and resistance, R_{xx} (right axis), at $B_z = 0$ to 0.5 T. The measurements are performed using the first voltage pair as in Fig. 2a. The plots are offset (except for $B_z = 0$ T) for a clearer visualization of the SdHOs. The red dashed line is to highlight the value of the $R_{xx} \approx 13$ kΩ at the charge neutrality point. **c** Conductance ($G = I/V_{xx}$) vs. V_{tg} close to the charge neutrality point at $B_z = 0$ T, measured in the four-terminal configurations shown in the schematics of the device in the inset (the graphene channel length and width are 6 and 2 µm, respectively). **d** Optical micrograph and schematics of device C that has two separate graphene channels with a different aspect ratio compared with that of devices A and B (the dimensions of the graphene channels are indicated in the schematics). The white dashed line in the optical image indicates the position where the graphene channel is cut to form two electrically isolated regions with 3 and 5 electrodes. **e** Two-, three- and four-terminal conductance in device C, measured at various configurations shown in the schematics of the device in the insets. Note that the V_{CNP} in device C is around 4–6 V. All measurements are performed at $B_z = 0$ T at $T = 2.3$ K. The dashed lines indicate the theoretically expected values for conductance considering helical states, color-coded with respect to the measurement geometry indicated in the inset.

point at V_{cnp}, implying finite shifts of the LLs in V_{tg}. We can correlate the shift of the LLs to the opening of the bulk gap at the charge neutrality point in the graphene channel due to the induced staggered potential. The shift is pronounced in the V_{tg}-dependence since the presence of the CPS midgap states within the graphene bulk gap and LL gaps slows down the tuning of the E_F close to the V_{cnp} (further details in SI, Section 9). It is also worth noting that the zLL shows minimal broadening and a negligible increase in resistance vs. B_z, in contrast to that reported in pristine graphene[14]. This observation is suggestive of the presence of edge states at the zLL gap that shunt the transport at V_{cnp}. The slow modulation of the E_F by V_{tg} within the zLL energy gap in this system can assist with resolving the edge states within the gap.

On another note, we highlight that the spin-splitting of the LLs with $N_{LL} \neq 0$ is not resolved within the broadening of the SdHOs in the Landau fan diagram of Fig. 2a. We attribute this to the presence of disorder in this system (with low charge carrier mobility), hindering the resolution of the spin-split bands at higher energies. In fact, the absence of the spin-split Landau fan diagram indicates that the induced magnetism is not large in this heterostructure, and thus the observation of the strong AH effect should be mainly due to a sizable SOC induced in the graphene channel. The larger induced SOC, as compared with the exchange interaction, is expected to result in the emergence of helical (and not chiral) states in this heterostructure[20]. In fact, depending on the relative strengths of Rashba SOC, Kane-Mele SOC, and magnetic exchange interactions, the system can transition between the QSH and QAH regimes[20].

For addressing the topological edge states in the graphene bulk gap, we focus on the transport close to zero energy. Helical states are spin-polarized electron- and hole-like bands within the bulk gap of the proximitized graphene[18] that counter-propagate at the edges of the graphene channel, as shown in the schematics of Fig. 3a. Figure 3b shows the gate-dependence of the graphene resistivity (ρ_{xx}, left axis) and resistance (R_{xx}, right axis) close to the charge neutrality point, for small applied magnetic fields ($B_z \leq 0.5$ T). The ρ_{xx} shows oscillations that develop into the SdHOs in the Landau fan diagram of Fig. 2a at higher B_z. The V_{tg} dependence of ρ_{xx} at $B_z = 0$ T (in Fig. 3b) has a wide peak at the charge neutrality point. When such four-terminal longitudinal measurements are evaluated in terms of conductance ($G = 1/R_{xx} = I/V_{xx}$), as shown in Fig. 3c for different voltage probe pairs, it becomes evident that the broadened resistance peak at V_{cnp} at 0 T is a plateau of conductance at $2\,e^2/h$. This quantized conductance at zero energy is evidence for the presence of counter-propagating spin-polarized helical states, as depicted in Fig. 3a.

To further explore the helical nature of the edge transport at $B_z = 0$ T, we investigate the effect of floating voltage probes on the conductance values at the V_{cnp} measured in various geometries. Helical charge transport occurs on both edges of the graphene channel with each edge hosting one spin-polarized state[46]. In this case, the voltage probes present along the edges alter the conductance between the source and the drain, since the charges do not maintain their spin when entering the probes. Thus, according to the Landauer-Büttiker formalism[47] (SI, Section 13), the two-terminal conductance G_{2T} in the presence of two counter-propagating (helical) edge states is given by the relation:

$$G_{2T} = \frac{e^2}{h}\left(\frac{1}{N_L+1} + \frac{1}{N_R+1}\right), \quad (1)$$

where N_L and N_R are the number of floating probes between the source and drain, along the left and right edges of the conductor. Similarly, the four-terminal conductance G_{4T} is given by

$$G_{4T} = G_{2T}\frac{N_I+1}{N_V+1}, \quad (2)$$

where N_I is the number of floating probes in between the source and drain along the edge which hosts the voltage probes, and N_V is the number of floating electrodes in between the voltage probes[48]. For the measurement of Fig. 3c, $N_L = N_R = N_I = 6$, and $N_V = 0$, thus, $G_{4T} = 2\,e^2/h$, which is the value measured at $B_z = 0$ T at the zLL conductance plateau. Considering the equations above, we evaluate the transport in various two-, three- and four-terminal measurement geometries, shown for device A in the SI, Figure S20, and for device C in Fig. 3e. The graphene channel in device C has been cut by an atomic force microscope tip, shaped into the Hall bar geometry with an aspect ratio different from that of device A and B, to rule out any coincidental geometrical factors in the measured conductance. Device C consists of two electrically disconnected regions with three and five electrodes connected to the channel (Fig. 3d). In panel e, the expected G values considering the helical edge states, following equations 1 and 2, are shown by the dashed lines that are color-coded with respect to each measurement geometry. We observe that, despite the distinct G measured at $V_{tg} \neq V_{cnp}$, the conductance values at V_{cnp} in each geometry closely match the theoretical values expected in the presence of QSH effect, confirming that the helical states dominate the charge transport at V_{cnp} in the magnetized graphene in the absence of an external magnetic field.

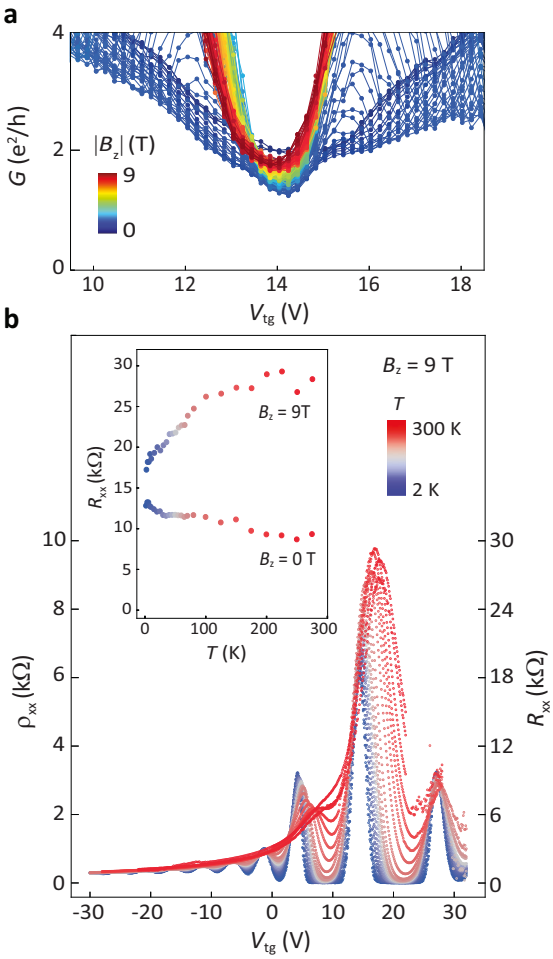

Fig. 4 | Magnetic field and temperature dependence of the QSH and QH transport. a V_{tg}-dependence of the conductance close to the V_{cnp}, measured at $0 < |B_z| < 9$ T in a four-terminal geometry with V_5 and V_6 voltage probes in device A. **b** Gate-dependence of the graphene resistivity (left axis) and resistance (right axis) at $B_z = 9$ T, measured at various T. Inset: Temperature-dependence of the maxima of the four-terminal resistance at $V_{tg} = V_{cnp}$, shown for $B_z = 0$, 9 T.

Under finite B_z, the conductance at the charge neutrality point in device A just slightly deviates from the quantized value of $2e^2/h$, as shown in Fig. 4a. Persistence of helical states at finite B_z depends on the evolution of the zLLs and can be disturbed by bands crossing at certain B_z[49]. In this case, the temperature dependence of the QH transport can provide further insight into the nature of the zLL gap[50]. In Fig. 4b, we show the gate-dependence of the graphene resistance at $B_z = 9$ T up to room temperature. We observe that the resistance at the zLL increases by increasing T. This metallic T-dependence is consistent with the presence of the gapless helical states at the zLL up to large B_z. In the inset of panel b, the $T-$ dependence of R_{xx} at zero energy is compared for $B_z = 0$ and 9 T. The slight decay of R_{xx} vs. T at $B_z = 0$ can be related to the scattering of the spin-polarized edge states at higher T due to random fluctuations of the magnetic moments (which is eliminated at large B_z). Thus, at $B_z = 0$ the contribution of the bulk transport becomes more dominant at higher T and the resistance drops as a result of the thermal broadening of the Dirac peak.

These observations introduce graphene-CPS heterostructure as a promising platform to exploit unconventional quantum phenomena for practical applications, as it hosts quantum coherent spin-polarized edge states without the need for any external magnetic field. The emergence of the QSH edge states is due to a strong hybridization at the graphene-CPS interface that induces spin-orbit and exchange interactions in graphene, further confirmed by the observation of a large AH effect. The coexistence of the AH and QSH effects in this system experimentally confirms the possibility of the formation of QSH states despite the breaking of time-reversal symmetry. The observation of helical states in graphene-based van der Waals heterostructures without an external magnetic field, in addition to the persistence of AH signal up to room temperature, opens the route for the direct applications of magnetic graphene in 2D topological spintronic devices.

Methods

$CrPS_4$ Synthesis

$CrPS_4$ crystals are grown following a solid-state reaction. Stoichiometric amounts of Cr (99.99%, Alfa-Aesar), P (>99.99%, Sigma-Aldrich) and S (99.99%, Sigma-Aldrich) are sealed inside an evacuated quartz tube (pressure 5×10^{-5} mbar, length: 50 cm, internal diameter: 14 mm) and placed in a three-zone furnace. A temperature gradient of 750/650/700 °C is kept for 21 days followed by a quench into water. The obtained crystals are analyzed by powder X-ray diffraction and energy-dispersive X-ray spectroscopy. The refinement of the X-ray pattern (ICSD 25059) reveals a monoclinic C face center crystal system with C121 space group and a unit cell determined by $\alpha = \gamma = 90°$ and $\beta = 91.99(1)°$ and $a = 10.841(9)\text{Å}$, $b = 7.247(6)\text{Å}$ and $c = 6.100(5)\text{Å}$. The amount of elements is Cr:23.3 ± 0.5%, P:14.8 ± 0.4% and S:61.8 ± 1.5%, in good agreement with the expected ones (Cr:24.6%, P: 14.7% and S: 60.7%). The obtained results are in accordance with the ones previously reported in the literature[39]. Note that the CPS flakes used in heterostructures with graphene in this work are from the same batch of crystal which is characterized by the SQUID magnetometry in Fig. 1b, c.

Electrical characterization

The charge transport measurements are performed using a DC current source, and voltages are measured using Keithley 2100 multimeters. DC voltage source is used for the gates. The measurements are performed using a variable temperature insert at He atmosphere (attoDry2100 system).

Data availability

The data generated in this study have been deposited in the Zenodo database open access [https://zenodo.org/records/15588027]. Additional data related to this paper may be requested from the corresponding author.

References

1. Neto, A. C., Guinea, F., Peres, N. M., Novoselov, K. S. & Geim, A. K. The electronic properties of graphene. *Rev. Mod. Phys.* **81**, 109 (2009).
2. Han, W., Kawakami, R. K., Gmitra, M. & Fabian, J. Graphene spintronics. *Nat. Nanotechnol.* **9**, 794–807 (2014).
3. Sierra, J. F., Fabian, J., Kawakami, R. K., Roche, S. & Valenzuela, S. O. Van der Waals heterostructures for spintronics and opto-spintronics. *Nat. Nanotechnol.* **16**, 856–868 (2021).
4. Wei, P. et al. Strong interfacial exchange field in the graphene/EuS heterostructure. *Nat. Mater.* **15**, 711–716 (2016).
5. Safeer, C. et al. Room-temperature spin Hall effect in graphene/MoS_2 van der Waals heterostructures. *Nano Lett.* **19**, 1074–1082 (2019).
6. Mendes, J. et al. Spin-current to charge-current conversion and magnetoresistance in a hybrid structure of graphene and yttrium iron garnet. *Phys. Rev. Lett.* **115**, 226601 (2015).
7. Ghiasi, T. S., Kaverzin, A. A., Blah, P. J. & Van Wees, B. J. Charge-to-spin conversion by the Rashba-Edelstein effect in two-dimensional van der Waals heterostructures up to room temperature. *Nano Lett.* **19**, 5959–5966 (2019).
8. Benítez, L. A. et al. Tunable room-temperature spin galvanic and spin Hall effects in van der Waals heterostructures. *Nat. Mater.* **19**, 170–175 (2020).
9. Wang, Z., Tang, C., Sachs, R., Barlas, Y. & Shi, J. Proximity-induced ferromagnetism in graphene revealed by the anomalous Hall effect. *Phys. Rev. Lett.* **114**, 016603 (2015).
10. Ghiasi, T. S. et al. Electrical and thermal generation of spin currents by magnetic bilayer graphene. *Nat. Nanotechnol.* **16**, 788–794 (2021).
11. Geim, A. K. & Grigorieva, I. V. Van der Waals heterostructures. *Nature* **499**, 419–425 (2013).
12. Yang, H.-X. et al. Proximity effects induced in graphene by magnetic insulators: first-principles calculations on spin filtering and exchange-splitting gaps. *Phys. Rev. Lett.* **110**, 046603 (2013).
13. Dyrdał, A. & Barnaś, J. Anomalous, spin, and valley Hall effects in graphene deposited on ferromagnetic substrates. *2D Mater.* **4**, 034003 (2017).
14. Young, A. F. et al. Spin and valley quantum Hall ferromagnetism in graphene. *Nat. Phys.* **8**, 550–556 (2012).
15. Young, A. et al. Tunable symmetry breaking and helical edge transport in a graphene quantum spin Hall state. *Nature* **505**, 528–532 (2014).
16. Veyrat, L. et al. Helical quantum Hall phase in graphene on $SrTiO_3$. *Science* **367**, 781–786 (2020).
17. Haldane, F. D. M. Model for a quantum Hall effect without landau levels: condensed-matter realization of the "parity anomaly". *Phys. Rev. Lett.* **61**, 2015 (1988).
18. Kane, C. L. & Mele, E. J. Quantum spin Hall effect in graphene. *Phys. Rev. Lett.* **95**, 226801 (2005).
19. Qiao, Z. et al. Quantum anomalous Hall effect in graphene from Rashba and exchange effects. *Phys. Rev. B* **82**, 161414 (2010).
20. Yang, Y. et al. Time-reversal-symmetry-broken quantum spin Hall effect. *Phys. Rev. Lett.* **107**, 066602 (2011).
21. Qiao, Z. et al. Quantum anomalous Hall effect in graphene proximity coupled to an antiferromagnetic insulator. *Phys. Rev. Lett.* **112**, 116404 (2014).
22. Kaloni, T. P., Kou, L., Frauenheim, T. & Schwingenschlögl, U. Quantum spin Hall states in graphene interacting with WS_2 or WSe_2. *Appl. Phys. Lett.* **105**, 233112 (2014).
23. Hatsuda, K. et al. Evidence for a quantum spin Hall phase in graphene decorated with Bi_2Te_3 nanoparticles. *Sci. Adv.* **4**, eaau6915 (2018).
24. Offidani, M. & Ferreira, A. Anomalous Hall effect in 2D Dirac materials. *Phys. Rev. Lett.* **121**, 126802 (2018).

25. Högl, P. et al. Quantum anomalous Hall effects in graphene from proximity-induced uniform and staggered spin-orbit and exchange coupling. *Phys. Rev. Lett.* **124**, 136403 (2020).
26. Vila, M., Garcia, J. H. & Roche, S. Valley-polarized quantum anomalous Hall phase in bilayer graphene with layer-dependent proximity effects. *Phys. Rev. B* **104**, L161113 (2021).
27. Bora, M., Behera, S. K., Samal, P. & Deb, P. Magnetic proximity induced valley-contrasting quantum anomalous Hall effect in a graphene-$CrBr_3$ van der Waals heterostructure. *Phys. Rev. B* **105**, 235422 (2022).
28. Obata, R. et al. Coexistence of quantum-spin-Hall and quantum-Hall-topological-insulating states in graphene/hBN on $SrTiO_3$ substrate. *Adv. Mater.* **36**, 2311339 (2024).
29. Song, H.-D. et al. Electrical control of magnetic proximity effect in a graphene/multiferroic heterostructure. *Appl. Phys. Lett.* **113** (2018).
30. Song, H.-D. et al. Asymmetric modulation on exchange field in a graphene/$BiFeO_3$ heterostructure by external magnetic field. *Nano Lett.* **18**, 2435–2441 (2018).
31. Wu, Y. et al. Large exchange splitting in monolayer graphene magnetized by an antiferromagnet. *Nat. Electron.* **3**, 604–611 (2020).
32. Wu, Y. et al. Magnetic exchange field modulation of quantum Hall ferromagnetism in 2D van der Waals $CrCl_3$/graphene heterostructures. *ACS Appl. Mater. Interfaces* **13**, 10656–10663 (2021).
33. Chau, T. K., Hong, S. J., Kang, H. & Suh, D. Two-dimensional ferromagnetism detected by proximity-coupled quantum Hall effect of graphene. *npj Quantum Mater.* **7**, 1–7 (2022).
34. Hu, J. et al. Tunable spin-polarized states in graphene on a ferrimagnetic oxide insulator. *Adv. Mater.* 2305763 (2023).
35. Wang, Y. et al. Quantum Hall phase in graphene engineered by interfacial charge coupling. *Nat. Nanotechnol.* 1–8 (2022).
36. Tseng, C.-C. et al. Gate-tunable proximity effects in graphene on layered magnetic insulators. *Nano Lett.* (2022).
37. Wang, X.-L. Dirac spin-gapless semiconductors: promising platforms for massless and dissipationless spintronics and new (quantum) anomalous spin Hall effects. *Natl Sci. Rev.* **4**, 252–257 (2017).
38. Lee, J. et al. Structural and optical properties of single-and few-layer magnetic semiconductor $CrPS_4$. *ACS Nano* **11**, 10935–10944 (2017).
39. Peng, Y. et al. Magnetic structure and metamagnetic transitions in the van der Waals antiferromagnet $CrPS_4$. *Adv. Mater.* **32**, 2001200 (2020).
40. Tang, C. et al. Approaching quantum anomalous Hall effect in proximity-coupled YIG/graphene/h-BN sandwich structure. *APL Mater.* **6** (2018).
41. Song, H.-D. et al. Anomalous Hall effect in graphene coupled to a layered magnetic semiconductor. *Phys. Rev. B* **103**, 125304 (2021).
42. Nagaosa, N., Sinova, J., Onoda, S., MacDonald, A. H. & Ong, N. P. Anomalous Hall effect. *Rev. Mod. Phys.* **82**, 1539 (2010).
43. Zhu, W. et al. Interface-enhanced room-temperature Curie temperature in $CrPS_4$/graphene van der Waals heterostructure. *Phys. Rev. B* **108**, L100406 (2023).
44. Novoselov, K. S. et al. Two-dimensional gas of massless Dirac fermions in graphene. *Nature* **438**, 197–200 (2005).
45. Zhang, Y., Tan, Y.-W., Stormer, H. L. & Kim, P. Experimental observation of the quantum Hall effect and Berry's phase in graphene. *Nature* **438**, 201–204 (2005).
46. Büttiker, M. Edge-state physics without magnetic fields. *Science* **325**, 278–279 (2009).
47. Büttiker, M. Four-terminal phase-coherent conductance. *Phys. Rev. Lett.* **57**, 1761 (1986).
48. Roth, A. et al. Nonlocal transport in the quantum spin Hall state. *Science* **325**, 294–297 (2009).
49. Böttcher, J., Tutschku, C., Molenkamp, L. W. & Hankiewicz, E. Survival of the quantum anomalous Hall effect in orbital magnetic fields as a consequence of the parity anomaly. *Phys. Rev. Lett.* **123**, 226602 (2019).
50. Abanin, D. A. et al. Dissipative quantum Hall effect in graphene near the Dirac point. *Phys. Rev. Lett.* **98**, 196806 (2007).
51. Diehl, R. & Carpentier, C.-D. The crystal structure of chromium thiophosphate, $CrPS_4$. *Acta Crystallogr. Sect. B: Struct. Crystallogr. Cryst. Chem.* **33**, 1399–1404 (1977).

Acknowledgements

We would like to acknowledge Yaroslav Blanter, Anton Akhmerov, Antonio Manesco, and Yafei Ren for insightful discussions. This project has received funding from the European Union Horizon 2020 research and innovation program under grant agreement, No. 863098 (SPRING). TSG acknowledges support from the Dutch Research Council (NWO) for a Rubicon grant (Project No. 019.222EN.013). J.I.-A. acknowledges support from the European Union's Horizon 2020 research and innovation programme for a Marie Sklodowska-Curie individual fellowship, No. 101027187-PCSV. K.W. and T.T. acknowledge support from the JSPS KAKENHI (Grant Numbers 21H05233 and 23H02052) and World Premier International Research Center Initiative (WPI), MEXT, Japan. S.M.-V. and E.C. acknowledge support from the European Union (ERC AdG Mol-2D 788222, FET OPEN SINFONIA 964396), and the Spanish MCIN (2D-HETEROS PID2020-117152RB-100 and Excellence Unit "María de Maeztu" CEX2019-000919-M). K.Z. and J.F. acknowledge support from DFG SFB1277 (Project No. 314695032) and SPP2244 (Project No. 443416183). P.K. acknowledges support by the Air Force Office of Scientific Research under award number FA2386-24-1-4073. H.S.J.v.d.Z. thanks the University of Valencia for a visitor grant.

Author contributions

T.S.G. and H.S.J.v.d.Z. conceived and designed the experiments. T.S.G. performed device fabrication and measurements with the help of D.P. T.S.G. and D.P. analyzed the data with the help of J.I.-A. T.B. and J.I.-A. assisted with measurements. S.M.-V. and E.C. synthesized the CPS crystals and performed the CPS magnetometry measurements. T.S.G. and P.K. further investigated the observations through fabrication and measurements of device C. K.W. and T.T. synthesized the hBN crystals. K.Z. and J.F. performed the DFT calculations. T.S.G. wrote the manuscript with contributions from all co-authors.

Competing interests

The authors declare no competing interests.

Additional information

Supplementary information The online version contains supplementary material available at https://doi.org/10.1038/s41467-025-60377-1.

Correspondence and requests for materials should be addressed to Talieh S. Ghiasi.

Peer review information *Nature Communications* thanks the anonymous reviewers for their contribution to the peer review of this work. A peer review file is available.